

A CONSISTENT STUDY OF METALLICITY EVOLUTION AT $0.8 < z < 2.6^*$

EVA WUYTS¹, JARON KURK¹, NATASCHA M. FÖRSTER SCHREIBER¹, REINHARD GENZEL^{1,2,3}, EMILY WISNIOSKI¹, KAUSHALA BANDARA¹, STIJN WUYTS¹, ALESSANDRA BEIFIORI^{1,4}, RALF BENDER^{1,4}, GABRIEL B. BRAMMER⁵, ANDREAS BURKERT⁴, PETER BUSCHKAMP¹, C. MARCELLA CAROLLO⁶, JEFFREY CHAN¹, RIC DAVIES¹, FRANK EISENHAEUER¹, MATTEO FOSSATI^{1,4}, SANDESH K. KULKARNI¹, PHILIPP LANG¹, SIMON J. LILLY⁶, DIETER LUTZ¹, CHIARA MANCINI⁷, J. TREVOR MENDEL¹, IVELINA G. MOMCHEVA⁸, THORSTEN NAAB⁹, ERICA J. NELSON⁸, ALVIO RENZINI⁷, DAVID ROSARIO¹, ROBERTO P. SAGLIA^{1,4}, STELLA SEITZ⁴, RAY M. SHARPLES¹⁰, AMIEL STERNBERG¹¹, SANDRO TACCHHELLA⁶, LINDA J. TACCONI¹, PIETER VAN DOKKUM⁸, AND DAVID J. WILMAN^{1,4}

¹ Max-Planck-Institut für extraterrestrische Physik, Giessenbachstr. 1, D-85741 Garching, Germany; evawuyts@mpe.mpg.de

² Department of Physics, Le Conte Hall, University of California, Berkeley, CA 94720, USA

³ Department of Astronomy, Hearst Field Annex, University of California, Berkeley, CA 94720, USA

⁴ Universitäts-Sternwarte München, Scheinerstr. 1, D-81679 München, Germany

⁵ Space Telescope Science Institute, Baltimore, MD 21218, USA

⁶ Institute of Astronomy, Department of Physics, Eidgenössische Technische Hochschule, ETH Zürich, CH-8093, Switzerland

⁷ Osservatorio Astronomico di Padova, Vicolo dell'Osservatorio 5, I-35122 Padova, Italy

⁸ Department of Astronomy, Yale University, P.O. Box 208101, New Haven, CT 06520-810, USA

⁹ Max-Planck Institute for Astrophysics, Karl Schwarzschildstrasse 1, D-85748 Garching, Germany

¹⁰ Department of Physics, Durham University, Science Laboratories, South Road Durham DH1 3LE, UK

¹¹ School of Physics and Astronomy, Tel Aviv University, Tel Aviv 69978, Israel

Received 2014 May 27; accepted 2014 June 17; published 2014 June 26

ABSTRACT

We present the correlations between stellar mass, star formation rate (SFR), and the $[\text{N II}]/\text{H}\alpha$ flux ratio as an indicator of gas-phase metallicity for a sample of 222 galaxies at $0.8 < z < 2.6$ and $\log(M_*/M_\odot) = 9.0\text{--}11.5$ from the LUCI, SINS/zC-SINF, and KMOS^{3D} surveys. This sample provides a unique analysis of the mass–metallicity relation (MZR) over an extended redshift range using consistent data analysis techniques and a uniform strong-line metallicity indicator. We find a constant slope at the low-mass end of the relation and can fully describe its redshift evolution through the evolution of the characteristic turnover mass where the relation begins to flatten at the asymptotic metallicity. At a fixed mass and redshift, our data do not show a correlation between the $[\text{N II}]/\text{H}\alpha$ ratio and SFR, which disagrees with the 0.2–0.3 dex offset in $[\text{N II}]/\text{H}\alpha$ predicted by the “fundamental relation” between stellar mass, SFR, and metallicity discussed in recent literature. However, the overall evolution toward lower $[\text{N II}]/\text{H}\alpha$ at earlier times does broadly agree with these predictions.

Key words: galaxies: evolution – galaxies: high-redshift – infrared: galaxies

Online-only material: color figures

1. INTRODUCTION

Observed relations between a galaxy’s stellar mass, star formation rate (SFR), and gas-phase metallicity can provide crucial constraints for galaxy evolution models that aim to understand the buildup of galaxies over cosmic time. The existence of a correlation between stellar mass and metallicity has been firmly established both locally (e.g., Lequeux et al. 1979; Tremonti et al. 2004), and out to $z = 3.5$ (e.g., Erb et al. 2006; Wuyts et al. 2012; Yuan et al. 2013; Zahid et al. 2013; Henry et al. 2013; Cullen et al. 2014; Steidel et al. 2014). Systematic uncertainties in the derivation of gas-phase metallicities from emission-line diagnostics significantly influence the absolute normalization and slope of the mass–metallicity relation (MZR; Kewley &

Ellison 2008), and they have complicated measurement of its evolution with redshift. Recently, it has been found that including SFR as a secondary parameter in the correlation greatly reduces the scatter in the local MZR (Ellison et al. 2008; Mannucci et al. 2010; Lara-López et al. 2010; Yates et al. 2012; Andrews & Martini 2013), though much less so at high redshift (e.g., Zahid et al. 2013; Steidel et al. 2014). Mannucci et al. (2010) proposed a fundamental metallicity relation between galaxy abundance, mass, and SFR that does not evolve with redshift out to $z = 2.5$. Theoretical studies ranging from analytic equilibrium models (e.g., Lilly et al. 2013) to cosmological hydrodynamical simulations (e.g., Davé et al. 2012; Hirschmann et al. 2013) offer their own predictions of the MZR and the correlation with SFR; comparisons with observations provide crucial constraints on the physical processes and assumptions included in these models.

At high redshift, metallicity studies have long been based on relatively small samples due to the inherent difficulties of near-IR spectroscopy. They furthermore often remain limited to a narrow redshift range, such that attempts to constrain redshift evolution of the mass–metallicity relation necessarily rely on a comparison of different sample selections and diagnostics at each epoch. In this Letter, we present a sample of

* Based on observations obtained at the Very Large Telescope (VLT) of the European Southern Observatory (ESO), Paranal, Chile (ESO program IDs 073.B-9018, 074.A-9011, 075.A-0466, 076.A-0527, 078.A-0660, 079.A-0341, 080.A-0330, 080.A-0339, 080.A-0635, 081.A-0672, 082.A-0396, 083.A-0781, 087.A-0081, 088.A-0202, 088.A-0209, 091.A-0126, 092.A-0082, and 092.A-0091) and at the Large Binocular Telescope (LBT) on Mt. Graham in Arizona. This work is further based on observations taken by the 3D-HST Treasury Program (GO 12177 and 12328) with the NASA/ESA Hubble Space Telescope, which is operated by the Association of Universities for Research in Astronomy, Inc., under NASA contract NAS5-26555.

222 galaxies over a wide redshift range $0.8 < z < 2.6$ and mass range $\log(M_*/M_\odot) = 9.0\text{--}11.5$, for which we observed the $H\alpha$ and $[N\text{ II}]$ emission with a combination of the multi-object LUCI spectrograph at the Large Binocular Telescope (LBT) in Arizona, and the SINFONI and KMOS integral field (IFU) instruments at the Very Large Telescope (VLT) in Chile. The large size and extended redshift coverage of this sample allow a consistent analysis of the correlations between stellar mass, SFR, and gas-phase metallicity as traced by $[N\text{ II}]/H\alpha$, as well as their cosmic evolution. We adopt the Chabrier (2003) initial mass function and a flat cosmology with $\Omega_M = 0.3$ and $H_0 = 70\text{ km s}^{-1}\text{ Mpc}^{-1}$.

2. OBSERVATIONS AND DATA REDUCTION

2.1. KMOS

The KMOS^{3D} survey is targeting a mass-selected sample of star-forming galaxies (SFGs) at $0.7 < z < 2.7$ in the COSMOS, GOODS-South, and UDS deep fields with the KMOS multi-object integral field spectrograph at the VLT (Sharples et al. 2013). Publicly available optical spectroscopic redshifts in these fields are supplemented with grism redshifts of all sources with $H_{140,AB} < 24$ mag from the 3D-HST Treasury Survey (Brammer et al. 2012). This results in a target sample with reduced bias toward blue, star-forming, dust-free galaxies, as is inherent to samples based solely on optical spectroscopic redshift. The galaxy sample studied in this Letter originates from commissioning data and the first semester of GTO observations, during which 105 unique targets at $\langle z \rangle = 0.9$ and 67 targets at $\langle z \rangle = 2.3$ were observed with median on-source integration times of 4 hr and 8.3 hr, respectively (E. Wisnioski et al. 2014, in preparation). The data were reduced using the Software Package for Astronomical Reductions with KMOS (SPARK; Davies et al. 2013).

The KMOS data cubes are analyzed with the custom tool *LINEFIT*, following the procedures described in detail by Förster Schreiber et al. (2009). We smooth each cube with a 3 pixel wide filter along the spatial axes. When the $H\alpha$ emission line is detected at $S/N > 3$ in an individual spatial pixel, we proceed to fit $H\alpha$ and $[N\text{ II}]$ simultaneously, forcing a common line width and redshift and locking the flux ratio of the $[N\text{ II}]$ doublet to its theoretical value of 3.071 (Storey & Zeppen 2000). With current integration times, we are able to derive a robust velocity field for 62/107 targets at $\langle z \rangle = 0.9$ and 47/67 targets at $\langle z \rangle = 2.3$.

2.2. LUCI

From 2009 December to 2012 May, we observed 148 SFGs at $1.3 < z < 2.5$ in the GOODS-North deep field and 8 SFGs at $z \sim 2.3$ in the Q2343 field (Steidel et al. 2004) with the multi-slit near-IR spectrograph LUCI at the LBT (Seifert et al. 2010) for a median integration time of 4 hr. Targets were purely selected on spectroscopic redshift, based on version 1.0 of the GOODS-N PEP multi-wavelength catalog (Berta et al. 2011). We employed 1" wide slits with the 210zJHK and 150 Ks gratings, which provide spectral resolutions of $R \sim 2900$ and $R \sim 1900$, respectively. The observations were reduced employing a custom pipeline developed at MPE, which includes bad pixel masking, cosmic-ray removal, distortion-correction, and optimal sky subtraction based on Davies (2007). For this work, we include 52 SFGs where $H\alpha$ is detected at $S/N > 3$, and the $H\alpha$ and $[N\text{ II}]$ lines are not contaminated by skylines.

2.3. SINS/zC-SINF

The SINS and zC-SINF surveys have observed >100 SFGs at $1.3 < z < 2.5$ with the near-IR IFU spectrograph SINFONI at the VLT (Eisenhauer et al. 2003), with on-source integration times ranging from 1 hr to more than 20 hr. Target selection, observations, and data reduction are described in detail by Förster Schreiber et al. (2009) and Mancini et al. (2011). Targets were selected from optical spectroscopic surveys of various parent samples photometrically selected based on rest-frame UV/optical magnitudes or colors. Thirty-five galaxies have been followed up with adaptive optics (N. M. Förster Schreiber et al. 2014, in preparation). Here, we use a subsample of 61 galaxies with robust kinematics; they are detected with $S/N = 23 \pm 12$ in $H\alpha$.

3. METHODOLOGY

3.1. SFR, Stellar Mass, and the $[N\text{ II}]/H\alpha$ Line Ratio

We derive the SFRs and stellar masses for our sample from a combination of 3D-HST grism spectroscopy (Brammer et al. 2012) with multi-wavelength rest-frame UV/optical photometry (Skelton et al. 2014) and far-IR photometry (available for 55% of our sample; Lutz et al. 2011; Magnelli et al. 2013), using standard spectral energy distribution fitting techniques and a ladder of SFR indicators (Wuyts et al. 2011). Our analysis of the gas-phase metallicities is carried out as much as possible in terms of the directly observable $[N\text{ II}]/H\alpha$ line ratio to avoid systematics associated with the choice of strong-line metallicity calibration (Kewley & Ellison 2008). When necessary, we employ the linear metallicity calibration by Pettini & Pagel (2004) to relate $[N\text{ II}]/H\alpha$ to the oxygen abundance $12 + \log(O/H)$,¹² which has an intrinsic dispersion of 0.18 dex.

For each KMOS and SINFONI data cube, we measure a global $[N\text{ II}]/H\alpha$ ratio from the galaxy-integrated one-dimensional (1D) spectrum within a maximal elliptical aperture positioned at the galaxy center, tilted along the kinematic position angle, and with an ellipticity that matches the outer $H\alpha$ isophotes. Within this aperture, the spectra of individual spatial pixels are co-added after being velocity-shifted to a common $H\alpha$ centroid based on the galaxy's velocity field. We detect $[N\text{ II}]$ at $S/N > 2$ for 61/62 KMOS targets at $\langle z \rangle = 0.9$ and 41/47 targets at $\langle z \rangle = 2.3$. For SINFONI, $[N\text{ II}]$ is detected at $S/N > 2$ for 10/12 targets at $\langle z \rangle = 1.55$ and 40/49 targets at $\langle z \rangle = 2.3$. The long-slit LUCI spectra are not corrected for the velocity structure of the source; we attempted this correction for a subset of the best-sampled targets and did not find a significant effect on the emission-line ratios. We measure $[N\text{ II}]$ at $S/N > 2$ for 12/14 LUCI targets at $\langle z \rangle = 1.45$ and 20/38 LUCI targets at $\langle z \rangle = 2.3$. For the 17% non-detections in our combined sample, we define 2σ upper limits on $[N\text{ II}]$ from the noise at the expected line position and the common linewidth.

3.2. AGN Contamination

We note that using $[N\text{ II}]$ emission as a metallicity indicator comes with its own complications, such as variations in the N/O ratio (Kennicutt et al. 2003) and saturation at high metallicities (Kewley & Dopita 2002). An important issue is the enhancement of $[N\text{ II}]/H\alpha$ for galaxies where an active galactic nucleus (AGN) contributes to the ionizing radiation or shocks affect the ionization balance (Kewley et al. 2013; Newman et al. 2014).

¹² $12 + \log(O/H) = 8.9 + 0.57 \times \log([N\text{ II}]/H\alpha)$.

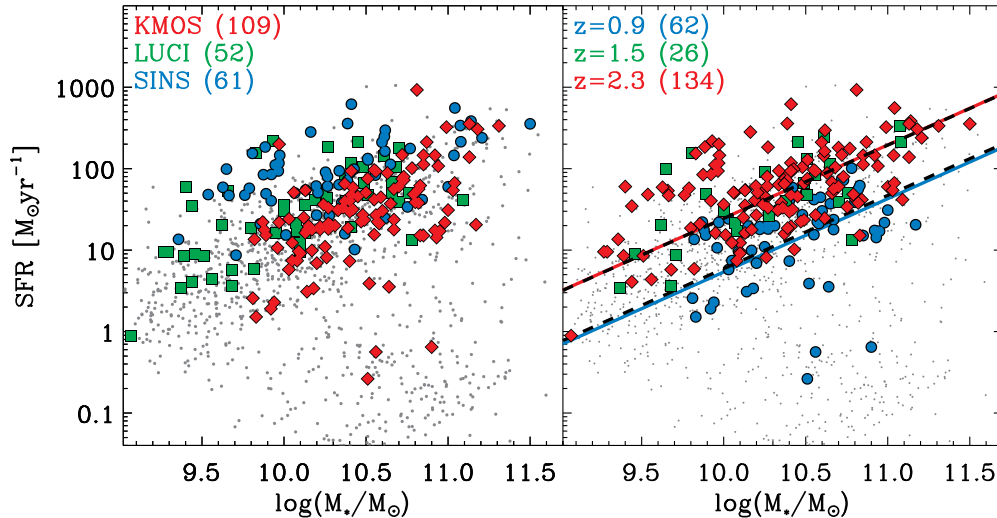


Figure 1. Location of our sample in the SFR–stellar mass diagram. We have color-coded the data points by instrument in the left panel and redshift in the right panel. The numbers in parentheses note the number of sources in each survey or redshift bin. As a reference, the small gray dots represent the mass-selected galaxy population at $0.7 < z < 2.7$ in the CANDELS/3D-HST fields. In the right panel, the blue and red solid lines show the star formation main sequence from Lilly et al. (2013) at $z = 0.9$ and $z = 2.3$, respectively. The dashed black lines represent the best-fit relations to our spectroscopic sample at these redshifts.

(A color version of this figure is available in the online journal.)

We identify 18 AGNs in our sample from X-ray and radio data, infrared colors, and rest-UV spectroscopy (see Genzel et al. 2014 for more details). Additionally, recent IFU studies have found evidence for an AGN in the central regions of massive $z = 1$ – 2 SFGs from broad outflow components and/or enhanced line ratios (Wright et al. 2010; Förster Schreiber et al. 2014; Newman et al. 2014). Genzel et al. (2014) report broad (FWHM $\gtrsim 1000$ km s $^{-1}$) emission components associated with the nuclear regions of 20 targets included in our combined sample.

3.3. Stacking

To include the $[\text{N II}]$ upper limits in our analysis, we stack the galaxies in bins of stellar mass. The 22 galaxies at $z = 1.5$ do not suffice for an analysis as a function of stellar mass and will therefore not be discussed further, though we note that stacking all $z = 1.5$ sources together results in an $[\text{N II}]/\text{H}\alpha$ ratio intermediate between the $z = 0.9$ and $z = 2.3$ samples and consistent with previous results in the literature (Figure 2). At $z = 0.9$ and $z = 2.3$, we stack galaxies in three or four mass bins, respectively, after removing the AGNs and galaxies with broad emission components from our sample. For each mass bin, the 1D source spectra are continuum-subtracted, de-redshifted, and normalized by the total $\text{H}\alpha$ flux. We exclude wavelength regions badly affected by skylines and robustly derive emission-line fluxes and uncertainties for the stacked spectra as the jack-knife mean and standard error. The median stellar mass and SFR and the stacked $[\text{N II}]/\text{H}\alpha$ ratio for each bin is reported in Table 1. At $z = 2.3$, we checked whether stacking each of the KMOS, LUCI, and SINS subsamples separately gives consistent results.

4. RESULTS

4.1. The Mass–Metallicity Relation

Figure 1 situates our sample in the SFR–stellar mass diagram and shows consistency with the star formation main sequence as parameterized by Lilly et al. (2013) at $z = 0.9$ and $z = 2.3$. In Figure 2, we show the galaxy-integrated $[\text{N II}]/\text{H}\alpha$ ratios for all sources as a function of their stellar mass. Symbols are

color-coded by redshift, and the mean uncertainty in $[\text{N II}]/\text{H}\alpha$ is ± 0.05 (ranging from 0.039 to 0.066 for the various bands and surveys). AGNs are shown with four-pointed stars and galaxies with broad outflow components are identified with surrounding black circles. The stacked results (which exclude the AGNs and broad emission galaxies) are shown with filled colored diamonds. For reference, we obtain consistent results when including all galaxies in the stacks, as shown with the open diamonds in the right panel. Thus, while it remains important to check, the $\sim 10\%$ AGN contamination of our sample does not have a significant effect on the derived MZR.

For comparison, the local MZR from Zahid et al. (2013) based on $[\text{N II}]/\text{H}\alpha$ is included, which agrees with the result from Kewley & Ellison (2008) once this is converted to the linear instead of the cubic metallicity calibration from Pettini & Pagel (2004). At high redshift, we compare with $[\text{N II}]/\text{H}\alpha$ based relations at $z = 1.6$ (Zahid et al. 2013), $z = 2.2$ (Erb et al. 2006),¹³ and $z = 2.3$ (Steidel et al. 2014). We find good agreement toward high stellar masses, and some variation in the slope at the low-mass end. This is likely due to differences in sample selection. Juneau et al. (2014) recently reported a steeper local MZR after applying an $\text{H}\alpha$ luminosity threshold to a sample of Sloan Digital Sky Survey (SDSS) galaxies. A common problem is the bias of high- z spectroscopic studies against red dusty objects, which, given the positive correlation between dust extinction and metallicity (e.g., Zahid et al. 2013), are generally metal-rich. A detailed comparison of the selection of the various high- z samples, including their rest-frame $U - V$ colors as a measure of extinction, would be very instructive for a better understanding of the varying slopes.

We provide fits to the MZR based on the parameterization introduced by Zahid et al. (2014),

$$12 + \log(\text{O}/\text{H}) = Z_0 + \log \left[1 - \exp \left(- \left[\frac{M_*}{M_0} \right]^\gamma \right) \right], \quad (1)$$

¹³ We use the current stellar masses re-derived by Zahid et al. (2013) instead of the total stellar masses reported by Erb et al. (2006).

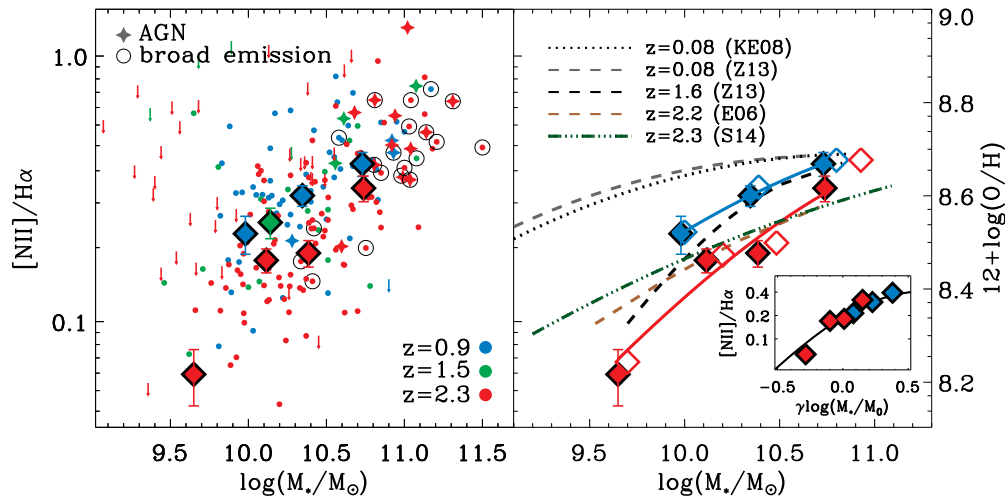


Figure 2. $[\text{N II}]/\text{H}\alpha$ flux ratio vs. stellar mass for our combined sample, color-coded by redshift. The left panel shows individual detections and 2σ upper limits. As explained in the text, AGNs identified from classic X-ray, etc., indicators and broad nuclear AGN-driven outflows are indicated with four-pointed stars and black circles, respectively. Large colored diamonds indicate the stacked $[\text{N II}]/\text{H}\alpha$ ratios in three, one, and four bins of stellar mass for the $z = 0.9$, $z = 1.5$, and $z = 2.3$ redshift slices, excluding the AGN-contaminated sources. The blue and red solid lines in the right panel correspond to our best-fit MZR as parameterized in Table 1. For reference, the open diamonds show the stacked results when all galaxies are included. We include the local MZR from Zahid et al. (2013) and Kewley & Ellison (2008), as well as relations from the literature at $z = 1.6$ (Zahid et al. 2013), $z = 2.2$ (Erb et al. 2006), and $z = 2.3$ (Steidel et al. 2014). The inset shows the stacked $[\text{N II}]/\text{H}\alpha$ ratios at $z = 0.9$ and $z = 2.3$ as a function of $\gamma \log(M_*/M_\odot)$ with fixed local slope $\gamma = 0.4$.

(A color version of this figure is available in the online journal.)

Table 1
Mass–Metallicity Relation

Redshift	Properties for Each Stellar Mass Bin				
	$\log(M_*/M_\odot)$	SFR	$[\text{N II}]/\text{H}\alpha$	No. of Targets	
$z = 0.9$	$9.98^{+0.16}_{-0.12}$	14^{+8}_{-11}	0.21 ± 0.03	18	
	$10.35^{+0.16}_{-0.13}$	19^{+21}_{-13}	0.30 ± 0.03	19	
	$10.73^{+0.17}_{-0.14}$	30^{+32}_{-15}	0.39 ± 0.04	19	
$z = 2.3$	$9.65^{+0.27}_{-0.16}$	40^{+71}_{-34}	0.06 ± 0.02	28	
	$10.11^{+0.12}_{-0.11}$	41^{+76}_{-28}	0.17 ± 0.02	28	
	$10.39^{+0.08}_{-0.06}$	64^{+41}_{-41}	0.18 ± 0.02	28	
	$10.74^{+0.13}_{-0.18}$	88^{+93}_{-47}	0.32 ± 0.04	29	
Best-fit Parameters					
Reference	Redshift	Z_0	$\log(M_0/M_\odot)$	γ	$\log(M_0^{\text{fixed}}/M_\odot)$
Z13	0.08	8.69 ± 0.01	9.02 ± 0.02	0.40 ± 0.01	8.95 ± 0.05
This work	0.9	8.8 ± 0.4	10.2 ± 0.9	0.4 ± 0.6	9.78 ± 0.11
This work	2.3	8.7 ± 0.3	10.5 ± 0.5	0.5 ± 0.2	10.36 ± 0.06

where Z_0 corresponds to the asymptotic metallicity, M_0 is the characteristic turnover mass where the relation begins to flatten, and γ is the power-law slope at stellar masses $\ll M_0$. Out to $z = 1.6$, Zahid et al. (2014) found a constant asymptotic metallicity and slope and a power law increase of M_0 with redshift, such that redshift evolution of the MZR depends solely on the evolution of the characteristic turnover mass. They suggest that this follows from the more fundamental universal relation between metallicity and stellar-to-gas mass ratio. Our best-fit parameters in Table 1 confirm this result within the uncertainties out to $z = 2.3$. The relation between metallicity and stellar mass scaled by M_0 is therefore independent of redshift, as can be seen in the inset in the right panel of Figure 2. The rightmost column in Table 1 reports the best-fit M_0^{fixed} derived for a fixed $Z_0 = 8.69$ and $\gamma = 0.40$ as found for the local relation. We can describe the redshift evolution of the

characteristic turnover mass as

$$\log(M_0/M_\odot) = (8.86 \pm 0.05) + (2.92 \pm 0.16) \log(1+z). \quad (2)$$

This result is not strongly dependent on the choice of Z_0 and γ . Zahid et al. (2014) report a consistent slope for $M_0(z)$ within the uncertainties; the difference in zero point is likely due to metallicity calibration offsets between the R23 and N2 indicators.

4.2. Star Formation Rate as a Secondary Parameter

We investigate the role of SFR in the mass–metallicity relation by stacking our sample at $z = 0.9$ and $z = 2.3$ in two bins of SFR for each mass bin. The left column of Figure 3 shows the 1σ dynamic range in SFR probed by each bin, as well as the median

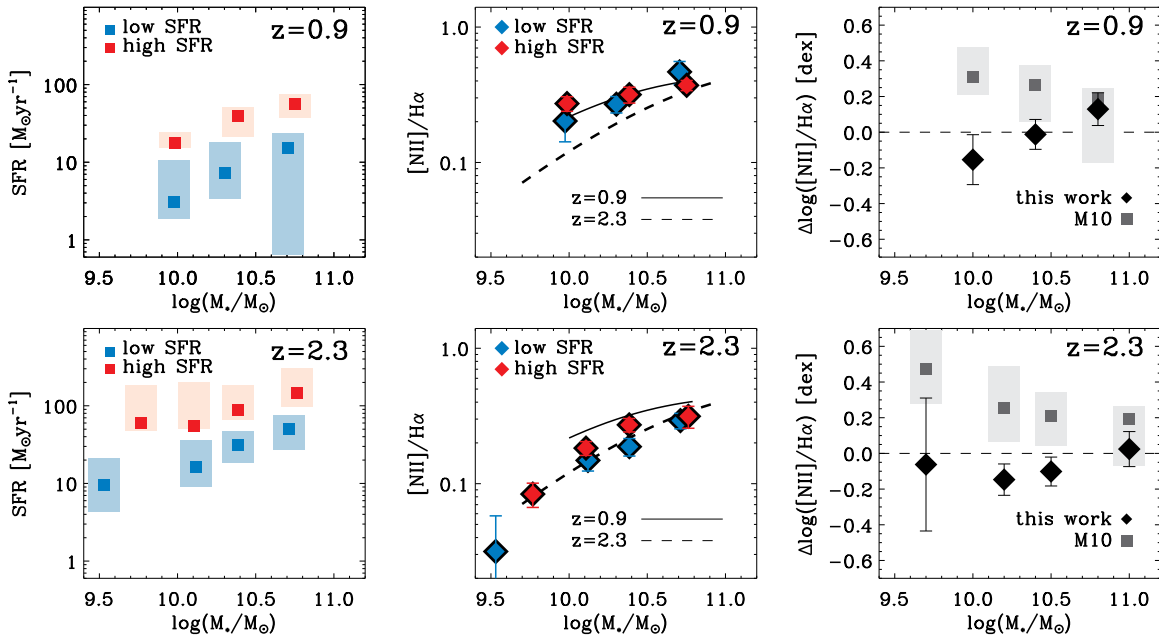


Figure 3. We divide the sample at $z = 0.9$ (top row) and $z = 2.3$ (bottom row) into two SFR bins for each stellar mass bin. In the left column, the shaded regions show the 1σ dynamic range in SFR probed in each bin; the filled square corresponds to the median value. In the middle column, the MZR for the low and high SFR bin is shown with blue and red diamonds, respectively. The black solid and dashed lines correspond to our best-fit MZRs at $z = 0.9$ and $z = 2.3$, as shown in Figure 2 and parameterized in Table 1. The MZR for each SFR bin is consistent with the best-fit MZR for the full sample at that redshift. Hence, at fixed mass and redshift we do not find a correlation between the [N II]/H α flux ratio and SFR. The right column shows the relative offset in $\log([\text{N II}]/\text{H}\alpha)$ between SFR bins $\Delta\log([\text{N II}]/\text{H}\alpha) = \log([\text{N II}]/\text{H}\alpha)_{\text{lowSFR}} - \log([\text{N II}]/\text{H}\alpha)_{\text{highSFR}}$. We compare our data (black diamonds) to the expectation from Mannucci et al. (2010) for the 1σ dynamic range in SFR for each bin (shaded regions).

(A color version of this figure is available in the online journal.)

value. As seen in the middle column, we do not find a correlation between the [N II]/H α ratio and SFR at fixed mass and redshift. The MZR for the low and high SFR bins is consistent with the best-fit MZR derived for the complete sample at that redshift. This result is confirmed when we split each mass bin into three bins of SFR and compare the top and bottom third. In contrast, Zahid et al. (2013) do find a correlation for their sample at $z = 1.6$. The range of SFR probed is similar to our sample, but they use dust-corrected H α -derived SFRs instead of the ladder of SFR_{UV+IR} used here. Using H α for both the SFR and metallicity measurement could introduce an artificial trend. Alternatively, the longer timescales probed by SFR_{UV+IR} might average out the correlation with gas-phase metallicity.

We compare our data to the fundamental relation between metallicity, stellar mass, and SFR proposed by Mannucci et al. (2010). Since their relation is based on the Maiolino et al. (2008) metallicity calibration, and our high- z sample probes significantly larger SFRs, one should be careful in interpreting a direct comparison. The shaded region in the right column of Figure 3 shows the relative metallicity offset predicted by Mannucci et al. (2010) for the 1σ dynamic range in SFR for our mass bins. The positive values for $\Delta\log([\text{N II}]/\text{H}\alpha) = \log([\text{N II}]/\text{H}\alpha)_{\text{lowSFR}} - \log([\text{N II}]/\text{H}\alpha)_{\text{highSFR}}$ reflect the anti-correlation between SFR and metallicity that they find for the SDSS sample, which becomes more pronounced at low stellar masses. In contrast, our data at fixed $z = 0.9$ and $z = 2.3$ show no relative offset in [N II]/H α between SFR bins, or even a somewhat negative one. In Figure 4 we directly plot metallicity versus $\mu = \log(M_*) - 0.32\log(\text{SFR})$, which has been proposed as the projection that minimizes the scatter in the local relation between metallicity, mass, and SFR. To be consistent, here we use the Maiolino et al. (2008) calibration to derive metallicities from our [N II]/H α ratios. We find an overall agreement with the

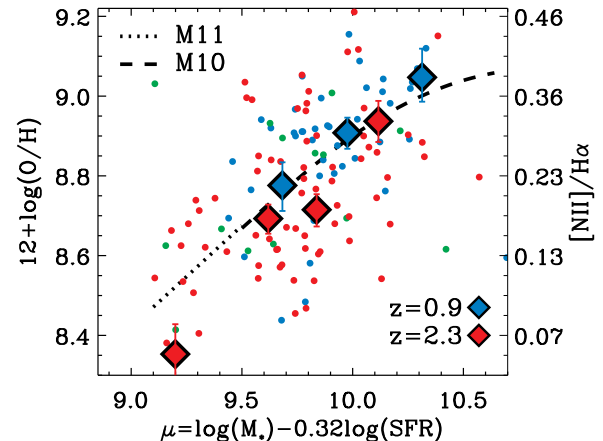


Figure 4. Metallicity derived from the Maiolino et al. (2008) calibration of the [N II]/H α flux ratio vs. $\mu = \log(M_*) - 0.32\log(\text{SFR})$ for individual targets and spectra stacked in bins of μ at $z = 0.9$ and $z = 2.3$. For comparison, we show the local relation from (Mannucci et al. 2010, dashed line) and the extension to lower stellar masses from (Mannucci et al. 2011, dotted line).

(A color version of this figure is available in the online journal.)

relation proposed by Mannucci et al. (2010) and their extension toward lower stellar masses (Mannucci et al. 2011), though there is some tension for the lowest mass bin.

5. SUMMARY

We report the [N II]/H α flux ratios for a sample of 222 galaxies at $0.8 < z < 2.6$, probing a wide range of stellar masses $\log(M_*/M_{\odot}) = 9.0\text{--}11.5$. The extended redshift coverage allows for the first consistent analysis of the evolution of the correlations between stellar mass, SFR, and gas-phase

metallicity with cosmic time. We detect [N II] for 83% of our sample and employ stacking techniques to extend the results down to $\log(M_*/M_\odot) = 10.0$ at $z = 0.9$ and $\log(M_*/M_\odot) = 9.7$ at $z = 2.3$. We find good agreement with other high- z MZR in the literature, though a careful analysis of sample selection is necessary to interpret the slope toward low stellar masses. Our results at $z = 0.9$ and $z = 2.3$ show a common power-law slope with the local MZR within the uncertainties, such that the redshift evolution of the MZR can be fully determined by the evolution of the characteristic turnover mass M_0 .

In the context of the “fundamental relations” between metallicity, stellar mass, and SFR that have been found locally, the redshift evolution of the MZR toward lower abundances at earlier times has been interpreted as being due to the higher SFRs of high- z SFGs. However, the lack of correlation between SFR and metallicity at fixed redshift and mass shown here, suggests that the redshift evolution of SFR and metallicity might not be causally related.

We are grateful to the referee for thoughtful comments that significantly improved the quality of this Letter. D.J.W. and M.F. acknowledge the support of the Deutsche Forschungsgemeinschaft via Project ID 387/1–1.

REFERENCES

- Andrews, B. H., & Martini, P. 2013, *ApJ*, **765**, 140
- Berta, S., Magnelli, B., Nordon, R., et al. 2011, *A&A*, **532**, A49
- Brammer, G. B., van Dokkum, P. G., Franx, M., et al. 2012, *ApJS*, **200**, 13
- Chabrier, G. 2003, *PASP*, **115**, 763
- Cullen, F., Cirasuolo, M., McLure, R. J., Dunlop, J. S., & Bowler, R. A. A. 2014, *MNRAS*, **440**, 2300
- Davé, R., Finlator, K., & Oppenheimer, B. D. 2011, *MNRAS*, **416**, 1354
- Davies, R. I. 2007, *MNRAS*, **375**, 1099
- Davies, R. I., Agudo Berbel, A., Wiezorrek, E., et al. 2013, *A&A*, **558**, A56
- Eisenhauer, F., Abuter, R., Bickert, K., et al. 2003, *Proc. SPIE*, **4841**, 1548
- Ellison, S. L., Patton, D. R., Simard, L., & McConnell, A. W. 2008, *ApJL*, **672**, L107
- Erb, D. K., Shapley, A. E., Pettini, M., et al. 2006, *ApJ*, **644**, 813
- Förster Schreiber, N. M., Genzel, R., Bouché, N., et al. 2009, *ApJ*, **706**, 1364
- Förster Schreiber, N. M., Genzel, R., Newman, S. F., et al. 2014, *ApJ*, **787**, 38
- Genzel, R., Förster Schreiber, N. M., Rosario, D., et al. 2014, arXiv:1406.0183
- Henry, A., Scarlata, C., Domínguez, A., et al. 2013, *ApJL*, **776**, L27
- Hirschmann, M., Naab, T., Davé, R., et al. 2013, *MNRAS*, **436**, 2929
- Juneau, S., Bournaud, F., Charlot, S., et al. 2014, *ApJ*, **788**, 88
- Kennicutt, R. C., Jr., Bresolin, F., & Garnett, D. R. 2003, *ApJ*, **591**, 801
- Kewley, L. J., & Dopita, M. A. 2002, *ApJS*, **142**, 35
- Kewley, L. J., Dopita, M. A., Leitherer, C., et al. 2013, *ApJ*, **774**, 100
- Kewley, L. J., & Ellison, S. L. 2008, *ApJ*, **681**, 1183
- Lara-López, M. A., Cepa, J., Bongiovanni, A., et al. 2010, *A&A*, **521**, L53
- Lequeux, J., Peimbert, M., Rayo, J. F., Serrano, A., & Torres-Peimbert, S. 1979, *A&A*, **80**, 155
- Lilly, S. J., Carollo, C. M., Pipino, A., Renzini, A., & Peng, Y. 2013, *ApJ*, **772**, 119
- Lutz, D., Poglitsch, A., Altieri, B., et al. 2011, *A&A*, **532**, A90
- Maiolino, R., Nagao, T., Grazian, A., et al. 2008, *A&A*, **488**, 463
- Magnelli, B., Popesso, P., Berta, S., et al. 2013, *A&A*, **553**, A132
- Mancini, C., Förster Schreiber, N. M., Renzini, A., et al. 2011, *ApJ*, **743**, 86
- Mannucci, F., Cresci, G., Maiolino, R., Marconi, A., & Gnerucci, A. 2010, *MNRAS*, **408**, 2115
- Mannucci, F., Salvaterra, R., & Campisi, M. A. 2011, *MNRAS*, **414**, 1263
- Newman, S. F., Buschkamp, P., Genzel, R., et al. 2014, *ApJ*, **781**, 21
- Pettini, M., & Pagel, B. E. J. 2004, *MNRAS*, **348**, L59
- Seifert, W., Ageorges, N., Lehmitz, M., et al. 2010, *Proc. SPIE*, **7735**, 256
- Sharples, R., Bender, R., Agudo Berbel, A., et al. 2013, *Msngr*, **151**, 21
- Skelton, R. E., Whitaker, K. E., Momcheva, I. G., et al. 2014, arXiv:1403.3689
- Steidel, C. C., Rudie, G. C., Strom, A. L., et al. 2014, arXiv:1405.5473
- Steidel, C. C., Shapley, A. E., Pettini, M., et al. 2004, *ApJ*, **604**, 534
- Storey, P. J., & Zeppen, C. J. 2000, *MNRAS*, **312**, 813
- Tremonti, C. A., Heckman, T. M., Kauffmann, G., et al. 2004, *ApJ*, **613**, 898
- Wright, S. A., Larkin, J. E., Graham, J. R., & Ma, C.-P. 2010, *ApJ*, **711**, 1291
- Wuyts, S., Förster Schreiber, N. M., Lutz, D., et al. 2011, *ApJ*, **738**, 106
- Wuyts, E., Rigby, J. R., Sharon, K., & Gladders, M. D. 2012, *ApJ*, **755**, 73
- Yates, R. M., Kauffmann, G., & Guo, Q. 2012, *MNRAS*, **422**, 215
- Yuan, T.-T., Kewley, L. J., & Rich, J. 2013, *ApJ*, **767**, 106
- Zahid, H. J., Kashino, D., Silverman, J. D., et al. 2013, arXiv:1310.4950
- Zahid, J., Dima, G., Kudritzki, R., et al. 2014, arXiv:1404.7526